

West Chester University
Digital Commons @ West Chester University

Chemistry

College of Arts & Sciences

2014

Bubbles: A review of their relationship to the formation of thin films and porous materials

Kurt W. Kolasinski

West Chester University of Pennsylvania, kkolasinski@wcupa.edu

Follow this and additional works at: http://digitalcommons.wcupa.edu/chem_facpub



Part of the [Materials Chemistry Commons](#)

Recommended Citation

Kolasinski, K. W. (2014). Bubbles: A review of their relationship to the formation of thin films and porous materials. *Mesoporous Biomaterials*, 1, 49-60. <http://dx.doi.org/10.2478/mesbi-2014-0003>

This Article is brought to you for free and open access by the College of Arts & Sciences at Digital Commons @ West Chester University. It has been accepted for inclusion in Chemistry by an authorized administrator of Digital Commons @ West Chester University. For more information, please contact wcressler@wcupa.edu.

Kurt W. Kolasinski*

Bubbles: A review of their relationship to the formation of thin films and porous materials

Abstract: Bubbles arise at the intersection of gases with other phases. Their role in the formation and applications of thin films and porous materials is complex. At times they are to be avoided. In other cases they are essential to the desired properties and outcomes. In many cases their function, form and production are misunderstood or disregarded. This review seeks to connect a diverse array of technical and fundamental aspects of bubbles so as to facilitate more control and understanding of their functions and utility.

Keywords: bubble, thin film, porous materials, surface chemistry, etching, structure formation, applied surface science, microcompartments, silicon, PDMS

DOI 10.2478/mesbi-2014-0003

Received October 17, 2014; revised December 3, 2014; accepted December 3, 2014

1 Introduction

The humble bubble. It may seem a frivolity since we probably all enjoyed playing in a bubble bath as children. We may have marveled at the stream of bubbles that was released when a salt crystal was dropped into a glass of beer. The bubbles in beer, sparkling wine and carbonated waters are not merely for show and a tingling mouth feel [1]. Bubbles affect the aromatic perception of sparkling beverages because their collapse releases CO₂ and volatile organic compounds to the air and within the mouth.


However, bubbles are anything but a mere distraction, particularly in the materials science. In a nuclear reactor or any other environment containing solids exposed to high-energy radiation, H and He can be generated within the bulk of materials. Because of their low solubility, they can agglomerate into bubbles that change the mechanical properties of their host including the formation of cracks

and pores [2]. Segregation of gases out of a liquid mixture to form bubbles is of extreme importance for the petrochemical industry [3] either from the perspective of creating polymer foams or in the case low molecular mass gaseous fractions separating from high molecular mass liquid fractions in petroleum reserves. Boiling heat transfer is used generically in domestic and industrial settings. Nonetheless, theoretical and empirical descriptions are incomplete due to a lack of understanding of the fundamental physics of bubble dynamics, and flow and heat transfer at appropriately small time and length scales [4]. A number of other areas in which bubbles are important have been detailed in several fine reviews [4–8].

Bubble formation, evolution and collapse are central to the phenomena of sonoluminescence and sonochemistry [8]. Both of these phenomena are driven by the high temperatures achieved in the wake of bubble collapse. High temperature (in excess of 5000 K) and pressure (exceeding 1000 atm) result from the conversion of the kinetic energy of a liquid or liquid-solid slurry into heating the contents of a bubble as it collapses. In combination with the rapid heating and cooling rates ($>10^{10}$ K s⁻¹) that are associated with acoustic cavitation and bubble collapse during ultrasonic irradiation, these conditions lead to the formation of a unique type of chemical reactor. Sonochemical reactions are capable of producing nanostructured metals, alloys, oxides, carbides and sulfides [9–11]. Of particular interest for biomaterials is the sonochemical production of protein microspheres pioneered by Suslick *et al.* [10]. Protein microspheres find applications as echo contrast agents for sonography, in magnetic resonance imaging, and for oxygen or drug delivery [10, 12]. Biodegradable chitosan microspheres can be produced sonochemically with or without the encapsulation of organic dyes [13]. Chiral mesoporous titania was produced by Gedanken *et al.* [14] by ultrasonication of an aqueous mixture after addition of a solution of a chiral chelated Ti compound with a surfactant (dodecylamine) dissolved in ethanol. Nanoparticles of Au can be loaded directly into mesoporous TiO₂ with ultrasonication [15].

Bubble dynamics is also of great importance in the cleaning of particulate matter from semiconductor

*Corresponding Author: Kurt W. Kolasinski: Department of Chemistry, West Chester University, West Chester, PA 19383 USA, E-mail: kcolasinski@wcupa.edu

 © 2014 K. W. Kolasinski, licensee De Gruyter Open.

This work is licensed under the Creative Commons Attribution-NonCommercial-NoDerivs 3.0 License.

wafers [16] and medical devices [8]. These bubbles are the result of cavitation. In cavitation, bubbles form after a transient stretching of the liquid by the mechanical action of an agitator or ultrasonic field, or by an increase of the local flow velocity. Thus, the key factor in cavitation is pressure variation in the fluid. The formation of bubbles during boiling occurs when the temperature exceeds the boiling point and is driven by a much different mechanism. Energy delivered by bubble collapse is harnessed in shock wave lithotripsy, a non-invasive technique that uses ultrasound to destroy kidney or bladder stones. Other medical application of bubbles [8, 17] include use as ultrasound contrast agents and in drug delivery and gene transfection in which ultrasound is used as the trigger to deliver a pharmaceutical payload.

Bubbles may also result from the introduction of gases into a liquid. Gases are often generated as a product of chemical and electrochemical reactions. Because of its low solubility in water, H_2 produced by a current of a just a few $mA\ cm^{-2}$ is sufficient to supersaturate water and cause the formation of bubbles [18]. This is an area of special interest for this review. A fascinating application of bubble dynamics is their use to propel nanoscale objects [19, 20].

Magnesium is a lightweight metal, the biomedical applications of which have been comprehensively reviewed by Hornberger *et al.* [21]. Surface modification of Mg alloys is important for controlling the corrosion rate to make these alloys suitable for use in implants and stents [22, 23]. Programming the rate of dissolution such that an implant disappears after tissue healing can potentially make Mg alloys a superior material for stents to support vascular walls [65]. The dissolution rate and surface morphology is influenced not only by the composition of the liquid in contact with the alloy, but also the flow of this liquid and the generation of gas bubbles produced during dissolution [23]. Thus, the formation of H_2 bubbles as a byproduct of biodegradation is dependent on the location of the implant within the body as this changes the physiological and chemical conditions to which the implant is exposed [27]. Functionalization of Mg with a protein such as albumin [24, 25] or a biodegradable polymer such as polycaprolactone [66] can be used to reduce corrosion and H_2 evolution [24, 25]. Reduction in H_2 bubble formation is desirable to avoid pathologies associated with gas embolism including tissue separation [26, 27].

We will look at the intentional and unintentional effects of bubbles in the formation of thin films and porous materials. This review begins with an introduction to the physics of bubble formation. It then proceeds to look at practical applications of bubbles with an emphasis on their role in a number of biochemical and biomedical ap-

plications. It also highlights how chemistry within micro-compartments may itself differ from chemistry in bulk solutions.

2 Bubble Formation

Here we seek to answer a number of questions: When do bubbles form? When do they detach from a surface? How big are they at detachment? Questions regarding how fast they rise and how they grow after detachment are addressed elsewhere [28, 29]. Classical heterogeneous nucleation theory on a flat surface was given a thermodynamic foundation by Volmer [30]. Fletcher generalized this to nucleation on a convex spherical surface [31], a problem that was only recently given a rigorous thermodynamic formulation [32].

2.1 Classical nucleation theory

The usual presentation of classical nucleation theory starts from a consideration of the change in Gibbs energy dG that occurs at constant temperature T and pressure p for an infinitesimal change of moles of the gas phase dn_g and liquid phase dn_l when a spherical droplet is in contact with its vapor. A detailed treatment can be found in chapter 9 of [33] and an insightful discussion can be found in chapter 23 of [34]. The droplet of radius R and surface area $A = 4\pi R^2$ is composed of a material with surface tension σ . However, here we wish to consider a bubble, which has a negative radius of curvature, forming inside of a liquid. This slightly complicates the formalism of the mathematics; therefore, below we will take R to be positive.

A transfer of moles from the liquid to the gas changes the radius of the bubble, and the accompanying change in Gibbs energy is given by

$$dG = \mu_l dn_l + \mu_g dn_g + \sigma dA, \quad (1)$$

where μ_l and μ_g are the chemical potentials of the liquid and gas, respectively. Conservation of mass couples the molar changes directly,

$$dn_l = -dn_g. \quad (2)$$

The number of moles of gas is given by the product of molar density of gas ρ_g and the volume of the bubble,

$$n_g = \rho_g \left(\frac{4\pi}{3} \right) R^3. \quad (3)$$

Differentiating we find $dn_g = 4\pi\rho_g R^2 dR$ and $dA = 8\pi R dR$, which upon substitution into Eq. 1 yields,

$$dG = 4\pi R^2 \left[\rho_g (\mu_g - \mu_l) + \frac{2\sigma}{R} \right] dR. \quad (4)$$

From the second law of thermodynamics, we know that the system is at equilibrium when $dG = 0$ and it will evolve spontaneously in the direction indicated by $dG < 0$. These conditions define the stability of the bubble of radius R according to Eq. 4. The chemical potentials are functions of T and p . They are always positive, as is σ . If we choose the temperature and pressure such that $\mu_l < \mu_g$, the behavior of the system is simple: $dG < 0$ can only be achieved by decreasing R , that is, with $dR < 0$. The bubble shrinks and disappears.

However, if we choose T and p such that the gas is more stable than the liquid, i.e., such that $\mu_g < \mu_l$, the behavior is not as clear cut. Now the two terms in brackets have opposite signs, and whether the bubble grows ($dG < 0$ with $dR > 0$) or shrinks ($dG < 0$ with $dR < 0$) depends on the relative magnitudes of these two terms. Furthermore there is a critical radius at which the system is metastable. Metastability is defined by $dG = 0$, but noting that the slightest change in R (caused by a fluctuation in n_l and n_g) tips the system toward instability. Setting Eq. 4 equal to zero and solving for the critical radius R^* we find,

$$R^* = \frac{2\sigma}{\rho_g (\mu_l - \mu_g)}. \quad (5)$$

The behavior of a bubble at a T and p where the gas is more stable than the liquid thus depends on the radius of the bubble. If $R = R^*$, the bracketed term in Eq. 4 vanishes, $dG = 0$ and the droplet is stable. If the bubble is smaller than the critical radius, the bracketed term in Eq. 4 is positive, $dG < 0$ when the bubble shrinks. If the bubble is larger than the critical radius, the bracketed term in Eq. 4 is negative, $dG < 0$ when the bubble grows.

We are now in a position to answer the question, why must a system be supersaturated for homogeneous nucleation to occur? The difference between the chemical potential of an ideal gas dissolved in an ideal solution at a mole fraction x_g and the chemical potential of an ideal gas dissolved at its equilibrium mole fraction x_g^{eq} at a reference p (chosen as 1 atm) is given by

$$\Delta\mu_g = RT \ln (x_g/x_g^{eq}). \quad (6)$$

Note that in Eq. 6, R is the ideal gas constant. Thus, two terms are often used to parameterize the degree of supersaturation. The saturation ratio is defined as

$$\alpha = x_g/x_g^{eq} \quad (7)$$

and the supersaturation is defined as

$$S = x_g/x_g^{eq} - 1 = \alpha - 1. \quad (8)$$

Whereas the time averaged density of the liquid is uniform, motions of the molecules in the liquid inherent to the Maxwell-Boltzmann distribution of velocities lead to fluctuations in the density at any point in time at any arbitrary location in the liquid. Another way to think of density fluctuations is that clusters of molecular vacancies form in the liquid. A cluster of vacancies leads to a low-density region that defines a bubble. Any bubble with a radius smaller than the critical radius is unstable and decays back to a uniform liquid. Any bubble larger than the critical radius will grow and remain as a bubble. At equilibrium, where $S = 0$, the chemical potential of the gas and the liquid are equal. The critical radius is infinite according to Eq. 5. The probability of forming an infinitely large bubble is infinitely small. The phenomena of supersaturation, supercooling and superheating are logical consequences for any system held strictly at equilibrium in the absence of impurities and any other interfaces, which can act as heterogeneous and nonclassical nucleation sites as defined below.

Eq. 4 shows us that the Gibbs energy is a function of the radius of the bubble. Indeed, $dG/dR = 0$ at $R = R^*$, and evaluation of the second derivative shows that the Gibbs energy has a maximum at the critical radius. The value of the Gibbs energy change at this maximum $\Delta^\ddagger G$ is the Gibbs energy of activation for the formation of a bubble of the critical radius. According to Boltzmann statistics, the number density of bubbles N_c that attain the critical radius at equilibrium is

$$N_c = N \exp \left(-\Delta^\ddagger G/k_B T \right) \quad (9)$$

where N is the total number density of molecules and k_B is the Boltzmann constant. The value of $\Delta^\ddagger G$ is found by substituting the value of R^* from Eq. 5 into Eq. 1 after integration, from which we obtain

$$\Delta^\ddagger G = \frac{4}{3}\sigma R^{*2} = \frac{16\pi\sigma^3}{3\rho^2 (\mu_l - \mu_g)^2}. \quad (10)$$

The activation barrier can be lowered from infinity at equilibrium by increasing the chemical potential of the gas. This is accomplished according to Eq. 6 by increasing the concentration of the dissolved gas beyond its equilibrium value, that is, by going to large values of the saturation S .

The rate of bubble formation is calculated from Eq. 9 by assuming that this rate is given by the rate at which one more molecule is added to the critical nucleus. We assume that diffusion-limited transport of molecules to the critical nucleus occurs characterized by a classical prefactor of $k_B T/h$, where h is the Planck constant, and a diffusion

barrier of $\Delta_{dif}G$. The rate of bubble formation is then given by the diffusion rate time the number density of critical nuclei

$$J = N (k_B T / h) \exp(-\Delta_{dif}G / k_B T) \exp(-\Delta^\ddagger G / k_B T). \quad (11)$$

The rate of formation is, therefore, related to the supersaturation S brought about by a gas p by [7],

$$J = A \exp\left(\frac{-16\pi\sigma^3}{3k_B T (Sp)^2}\right). \quad (12)$$

From classical nucleation theory we learn that the nucleation of one phase in another occurs after the formation of a growth nucleus of a critical size R^* , which is opposed by an activation barrier $\Delta^\ddagger G$. This is why phenomena such as superheating and supersaturation can occur. Because of the difficulty of nucleating a new phase, nucleation almost never occurs homogeneously in a practical environment. Special circumstances such as large supersaturation, extreme purity and smoothness of interfaces must be constructed to facilitate homogeneous nucleation. For instance, homogeneous nucleation has been observed by created a single nanopore. The electrolyte contained in this pore was then subjected to Joule heating concentrated at the center of the pore. The centrally located temperature maximum ensured the homogeneous nucleation of a gas bubble in the center of the nanopore [35].

2.2 Classical versus nonclassical nucleation

Four types of nucleation have been defined [6], as shown in Fig. 1 specifically for the case of a gas bubble forming in a liquid. Type I nucleation is classical homogeneous nucleation: spontaneous growth of a bubble of gas within a supersaturated liquid following a density fluctuation. Type I nucleation typically requires supersaturation in excess of 100 to occur. Type II nucleation is classical heterogeneous nucleation: spontaneous growth at a liquid/solid interface (either with a random particulate or a container wall) within a supersaturated liquid following a density fluctuation. However, most studies on nucleation report rates in excess of the predictions of classical nucleation theory. The difficulties that classical nucleation theory has to describe bubble formation rates in real systems are both intrinsic and practical. As pointed out by Lubetkin [7], the conditions required to make a surface conducive to nucleation of bubbles are exactly the conditions required to make detachment of the bubbles difficult. Furthermore, extreme care must be taken to avoid the inclusion of gas filled cavities within a liquid. These cavities may either be metastable cavities with radii less than the critical nucleus

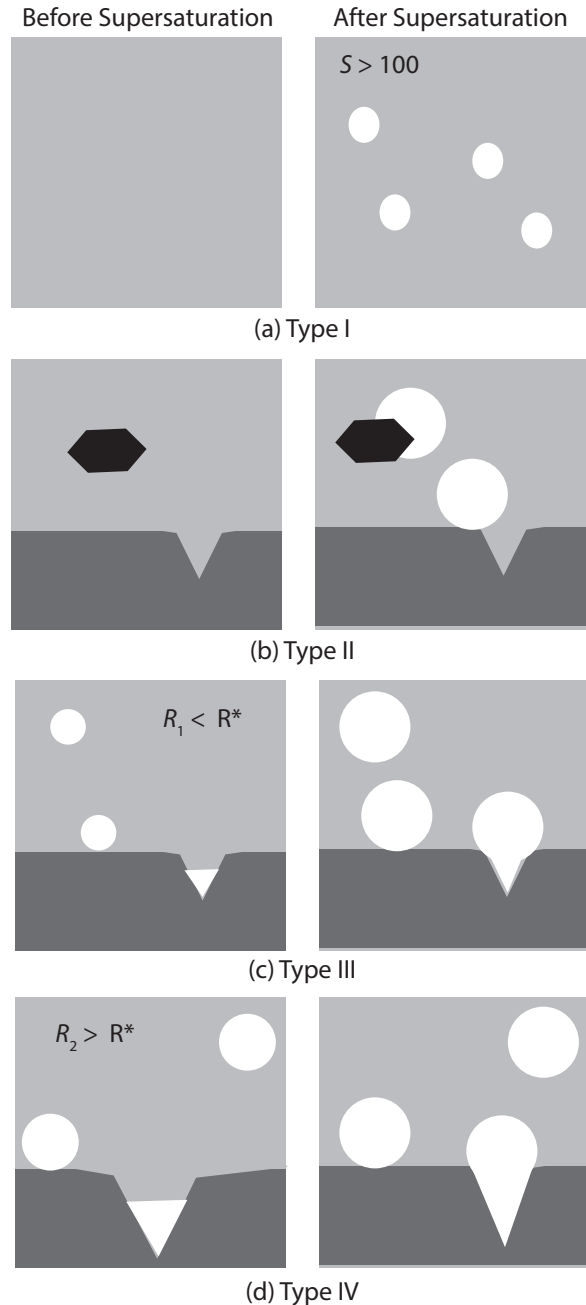


Figure 1: (a) Type I, (b) type II, (c) type III, and (d) type IV nucleation. S is the value of supersaturation. R_1 and R_2 are radii of curvature. R^* is the critical radius of nucleation. Redrawn after Jones, Evans and Galvin [6]. The black hexagonal object represents a random irregular particle suspended in the liquid. White regions represent gas-filled cavities. Before supersaturation such cavities only exist in the type III and type IV nucleation scheme. After supersaturation, these cavities are the bubbles that have nucleated and grown.

radius (Fig. 1(c) Type III nucleation) or they may be stable gas filled cavities (Fig. 1(d) Type IV nucleation). In either case, the cavities may exist either within the liquid or attached to a solid surface.

The circumstances of practical experiments have led us to the introduction of two additional types of nucleation. Type III nucleation is also called pseudo-classical nucleation. It occurs on metastable subcritical nuclei within the bulk of the liquid or attached to a surface. Type IV nucleation is called nonclassical nucleation since no activation energy is required for it to occur. It occurs at stable nuclei that are larger than the critical radius. You may have often noticed that bubbles stream away from a fixed point on the bottom or side of a glass containing a carbonated beverage. This is the result of Type IV nucleation at a scratch/crevice on the surface of the glass. Type IV nuclei will almost always form when a liquid is poured into a vessel unless precautions, as described in the work of Liger-Belair *et al.* below, are taken.

To illustrate the importance and ubiquitousness of Types III and IV nucleation, take the case of champagne. Liger-Belair *et al.* [1, 36, 37] have thoroughly studied the properties of bubbles in champagne wines. They instituted a rigorous cleaning strategy in which glasses were thoroughly washed in dilute aqueous formic acid, rinsed using distilled water, and then dried with compressed air. This treatment suppresses the formation of CaCO_3 crystals on the glass wall as well as the adsorption of dust particles that might act as nucleation sites. The sparkling wine is still contained within a glass; however, the smooth and clean wine/glass interface is unable to promote bubble formation. The sparkle is lost because at a supersaturation of only $S \sim 4$, as is common with champagne wines, neither classical homogeneous nor classical heterogeneous nucleation occur at an appreciable rate. Laser etching of the glass in a flute can be used to produce sites for Type IV nucleation. These findings are in complete harmony with the conclusion [6] that nucleation observed in most instances, corresponding to supersaturation of $S \leq 5$, is invariably associated with the existence of metastable gas cavities in the walls of the container or the bulk of the solution, prior to the system being made supersaturated.

2.3 Growth and detachment

The rate at which bubbles form in a real system depends on the number of nonclassical nucleation sites. It also depends on the transport of dissolved gas to these sites. The growth and detachment of bubbles from these sites is governed by classical arguments. Fig. 2 displays the growth to near detachment of an air bubble generated above an orifice in pure water. The bubble first assumes a near hemispherical shape. Gradually a nearly spherical upper portion begins to separate from the surface forming a neck

between the spherical portion and the bubble foot. Thus, three radii need to be distinguished as shown in Fig. 3. The contact radius r_0 (the radius of the bubble foot) stays constant and is the same as the orifice diameter. Counting up from the bottom, the radii of curvature of the neck and the spherical portion R_1 and R_2 , respectively.

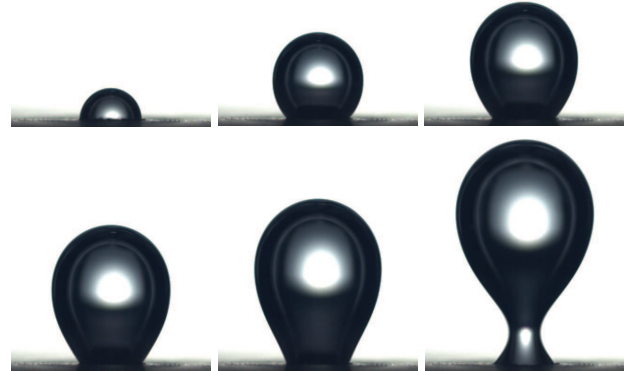


Figure 2: Growth and detachment of air bubbles from an orifice submerged in ultrapure degassed water. Reproduced with permission from Albadawi *et al.* [5].

Modeling this system and to answer the questions of when does a bubble detach and how large is a bubble at detachment, we will obtain a result close to that of Tate's law of bubble detachment [33]. This simple model of bubble detachment treats a spherical bubble for which forces generated by surface tension resist buoyancy forces. Fig. 2 shows that this is not an exact approximation; however, the result is not a bad approximation for very small bubbles. To more accurately model bubble detachment, we follow the analysis of Di Bari and Robinson closely [4]. First we make a series of simplifying assumptions in order to quantify the forces acting on the bubble:

1. Temperature is constant as are all fluid properties.
2. Bubble growth is occurring adiabatically and axis symmetrically.
3. The rate of change of vertical momentum of the gas bubble is negligible compared with the magnitude of the vertical forces acting on it.
4. The gas pressure is uniform within the bubble, and the gas viscous and inertia influences are negligible.
5. The contact line remains fixed to the rim of the orifice.

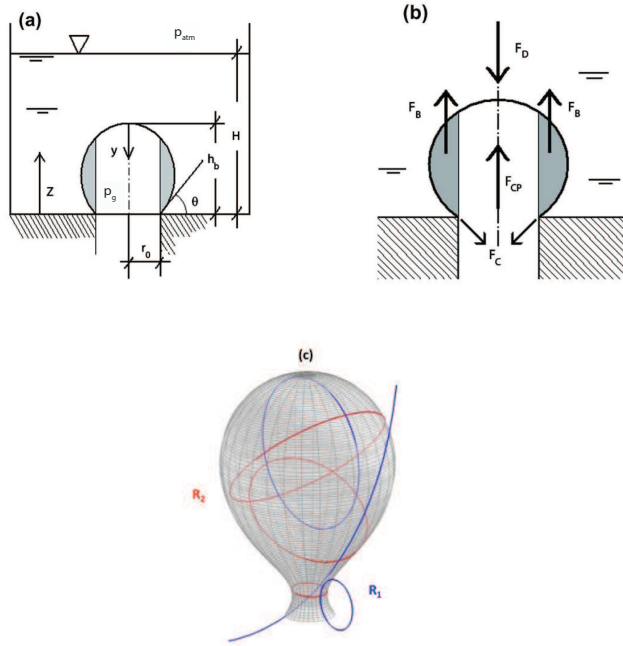


Figure 3: Representation of bubble nucleated at a cavity/orifice. The z axis is perpendicular to the solid surface to which the bubble is attached. Symbols are defined as follows: atmospheric pressure is p_{atm} ; the gas pressure within the bubble is p_g ; y is the vertical distance from the bubble apex; r_0 is the contact radius (bubble foot radius); θ is the contact angle; h_b is the bubble height; H is the liquid height; partial buoyancy force, F_B ; the contact pressure force, F_{CP} ; the capillary or surface tension force, F_C ; and the dynamic force, F_D . Reproduced with permission from Di Bari and Robinson [4].

Applying the above assumptions reduces the momentum balance on the bubble to what can be considered an equilibrium force balance of the form

$$\sum F = F_B + F_{CP} + F_C + F_D = 0. \quad (13)$$

The principle forces acting on the bubble are the partial buoyancy force, F_B , the contact pressure force, F_{CP} , the capillary or surface tension force, F_C , and the dynamic force, F_D . Each of these will be defined below. The specific case treated here is that of air injected into water from an orifice. This is analogous to the case of gas emerging from a pore, the gas having been generated by the etching reaction that formed the pore. As long as the bubble growth is sufficiently slow such that we need not consider liquid inertia, the analogy extends to any bubble growing on a surface from a fixed nucleation site.

The bubble contact diameter for-air-in water bubbles was studied by [4], who found that the bubble foot diameter remained fairly constant during the bubble lifetime. As a result, the upwardly directed net hydrostatic force, or

partial buoyancy force F_B , only acts on the volume which exists in the region radially outward from the triple contact line, i.e., the shaded grey region in Fig. 3. This is called the partial buoyancy force in order to avoid confusion with the classical definition posed by Archimedes. The partial buoyancy force is defined as,

$$F_B = \rho_l g V_B, \quad (14)$$

where V_B is the volume section of the bubble with liquid both above and below it, ρ_l is the liquid density, and g is the acceleration due to gravity. For the case when a bubble neck has formed beneath the bubble, V_B is determined from the section existing above the minimum neck radius.

The contact pressure force F_{CP} is due to the action of the overpressure inside the bubble acting on the projected area of the bubble tip above the orifice. It is expressed in terms of the gas pressure p_g , liquid pressure at the bubble tip p_T , and the contact radius r_0 as

$$F_{CP} = \pi r_0^2 (p_g - p_T). \quad (15)$$

The choice of using p_T in Eq. 15 simplifies the calculation of the integral of the liquid pressure acting on the upper region of the bubble. We will see below that the contribution of F_{CP} can be neglected for nano- and meso-pores.

The capillary force F_C is a downwardly directed force that tends to keep the bubble attached to the wall. It arises due to capillary action at the triple interface and is related to the contact perimeter of the bubble and contact angle,

$$F_C = 2\pi r_0 \sigma \sin \theta, \quad (16)$$

where σ is the liquid surface tension and θ is the contact angle at the triple contact line.

Finally, the dynamical influence of the moving liquid adjacent to the gas-liquid interface in the second term of Eq. 13 is a result of inertial and viscous effects. For convenience, it is grouped into a single force term called the dynamic force,

$$F_D = F_{inertia} + F_{viscous}. \quad (17)$$

Fig. 3(b) illustrates the forces schematically. The dynamic force can be estimated provided that there is sufficient information available to calculate all of the other forces,

$$F_D = F_C - (F_{CP} + F_B). \quad (18)$$

The magnitude of the pressure difference across the curved gas-liquid interface is characterized by the Young-Laplace equation:

$$\Delta p = \sigma \left(\frac{1}{R_1} + \frac{1}{R_2} \right), \quad (19)$$

where Δp is the local difference of pressure, while R_1 and R_2 are the principal radii of curvature as defined in Fig. 3(c). The hydrostatic force acting on the bubble increases in the direction of the gravitational field causing the bubble shape to deviate from a perfect spherical section. The shape of a bubble in a gravitational field is governed by the capillary equation,

$$\sigma \left(\frac{1}{R_1} + \frac{1}{R_2} \right) = \frac{2\sigma}{R_T} - (\rho_l - \rho_g)gy, \quad (20)$$

where R_T is the radius of curvature at the tip of the bubble, ρ_l and ρ_g are the density of the liquid and the gas, respectively, g is the acceleration due to gravity and y is the vertical distance from the bubble apex.

The pressure inside the bubble p_g was measured [4] and is given by

$$p_g = \Delta p_m + p_{atm}, \quad (21)$$

where Δp_m is the measured differential pressure and p_{atm} is the atmospheric pressure. The local static pressure in the liquid at a vertical distance y from the bubble tip is

$$p_{ls} = p_{atm} + \rho_l g(H - h_b) + \rho_l g y, \quad (22)$$

where the first two terms account for the hydrostatic head between the free liquid surface and the apex of the bubble. Neglecting the gas inertia and substituting terms into the Young-Laplace equation, the local dynamic pressure can be estimated with

$$p_D = \Delta p_m - p_l - \sigma(1/R_1 - 1/R_2), \quad (23)$$

where $p_l = \rho_l g(H - h_b) + \rho_l g y$ represents the hydrostatic component of the local pressure.

The bubble growth develops in three stages. In the first stage, the bubble emerges as a sphere from the orifice. Progressively buoyancy acts upon a larger portion of the bubble. This brings the bubble into an elongation/expansion stage in which the bubble foot is fixed to the orifice mouth while buoyancy lifts the upper portion of the bubble. The rate of change of the center of gravity is constant in time during this stage.

The detachment stage begins with the formation of a neck near the bubble base. Buoyancy is enhanced by neck formation and leads to acceleration of the center of gravity. The collapse of the neck increases the rate of the necking process because it increases the influence of buoyancy yet more. Finally, the neck can resist no longer and the bubble detaches.

The relative contribution of the contact pressure force F_{CP} diminishes with orifice diameter. Di Bari and Robinson found that for an orifice < 0.6 mm in diameter, it plays a minor role at departure. Therefore it is of no importance for

bubbles emanating from nano- and meso-pores. This being the case, the departure volume will approach the Tate volume V_T . The Tate volume is derived from a balance of buoyancy and capillary forces with a departure contact angle in the region of 90° according to

$$V_T = \frac{\pi d_0 \sigma}{(\rho_l - \rho_g)g}. \quad (24)$$

The deviation of the detachment volume from V_T increases with increasing orifice size. Up to 0.2 mm or so, the difference is negligible for bubbles formed in water. More generally stated for any fluid [38], spherical bubbles are formed at low values of the Bond number, $Bo = \rho g R^2 / \sigma$.

3 Applications

Gas evolution during chemical or electrochemical reaction leads to a blanketing effect. If the bubbles are not removed they exclude contact of the solution with the surface. On the other hand, the motion of bubbles through a solution can stir the solution extremely effectively. Therefore, industrial electrolytic reactors are often designed to take advantage of this phenomenon by introducing a narrow gap between two electrode surfaces. This enhances the removal of the bubbles from the surfaces and leads to what is termed gas-lift electrolyte circulation [39]. A similar effect can be built into the design of laser induced backside wet etching cells [40].

A common reaction that is influenced by the formation of bubbles is the texturization of Si solar panels by KOH etching. This etching reaction is used to decrease reflectivity by the introduction of controlled surface roughness. On the other hand, in many micromachining applications smooth surfaces are required. Surface roughness is mainly controlled by conditions within the KOH etching solution, and in particular to the hydrogen gas bubbles evolved during etching [41]. Isopropyl alcohol is commonly added as a surfactant to aid in the removal of H_2 bubbles from the Si surface [42, 43]. Surface roughness after etching of Si in tetramethyl ammonium hydroxide (TMAH) can be substantially reduced when appropriate surfactants are added [44].

The etching of extremely flat Si(111) in $NH_4F(aq)$ solutions is relatively easy compared to the difficulty in obtaining comparably flat Si(100) surfaces. Part of the reason for this can be traced back to bubble dynamics [45–47]. Aldinger *et al.* proposed two new mechanisms of surface roughening during etching that involve bubbles. In the first mechanism, elevated but flat topped structures are formed by bubbles that adhere to the surface and grow lin-

early in time. The roughness is mainly confined to the ring of attachment. The second mechanism produces much more roughness. This process is driven by bubble coalescence followed by removal from the surface, which results in pitting and roughening.

Pauric *et al.* [48] have developed a technique for the formation of thin (on the order of $1\ \mu\text{m}$) porous metal films that may be interesting for applications ranging from catalysts and electrodes to sensors or biomaterials. Porous metal layers were produced on copper, silver, iron and nickel using 99% phosphoric or sulfuric acid. Such highly concentrated electrolytes are required because of the need to satisfy necessary conditions including high viscosity, high conductivity and a low water concentration. Anodization was performed for 4–30 min at voltages of 4–11 V where O_2 evolution becomes significant. The mechanism is not believed to involve specific chemistry; rather, it relies on templated etching due to a near-stagnant bubble layer in the viscous electrolyte.

The agglomeration of bubbles within a solid has been exploited to produce thin films, as described in detail by Moutanabbir and U. Gösele [49]. Hydrogen or He can be implanted at a controlled energy into semiconductor or ionic crystals. By controlling the incident energy, the depth of implantation is also controlled. Subsequent annealing of the substrate heals damage induced by the ion impacts and also forces the atoms to coalesce into void spaces within the solid. Those pockets of gas that are too close to the surface could lead to blistering or may even be able to form pores that facilitate escape of the gas. However, if the implantation depth is sufficiently deep, as when the energy is 1–4 MeV, or if a handle wafer is bonded to the upper interface, the gas filled cavities extend parallel to the interface. When conditions are favorable, cleavage and transfer of the upper thin film layer onto the handle wafer occurs. The thickness of transferred films can range from a few hundred nanometers to more than $17\ \mu\text{m}$.

In a related vein, several schemes for the transfer of graphene layers have been developed which rely upon the production of H_2 bubbles to remove the graphene from the substrate upon which it was grown [50–52].

Bubbles in the form of foaming agents have been used to produce a variety of porous solids. Such methods, as well as other synthetic methods, have been reviewed by Chevalier *et al.* [53] with special emphasis on applications in biomaterials and tissue engineering. Below I review two recent methods of producing materials with regular arrays of cavities that are useful in bioanalytical and biochemical applications.

Shang *et al.* [54] have described a technique reminiscent of blistering for the formation of microcavities and

channels, which they call a chemical foaming process. Their results showed that wafer-level micro-glass cavities with smooth wall surfaces were produced. Such cavities are suitable for use as micro-reactors, micro total analysis systems, microelectromechanical systems packaging, and in analytical and bio-analytical applications.

In the first step, 10–70 μm deep microcavities were fabricated by wet etching a 4-inch Si wafer with TMAH. This defines the pattern of the Si cavities and channels. Critical dimensions of the drawn features were from 100–3000 μm .

Second, TiH_2 was introduced from solution with a microinjector into a cavity as the foaming agent. TiH_2 was chosen because it has been used previously in preparing metal foams. Third, a 4-inch Pyrex7740 glass wafer (300–400 μm thick) was bonded anodically under vacuum to the patterned Si wafer to seal all the microcavities. Fourth, the bonded wafer was placed in a furnace set to 830–900°C, and kept for 1–10 min. Hydrogen released by thermal decomposition of TiH_2 pressurizes the cavities and deforms the softened glass into spherical and cylindrical shapes. Finally, the wafers were cooled and annealed according to a protocol to alleviate thermal stress. Examples of the structures formed are shown in Fig. 4.

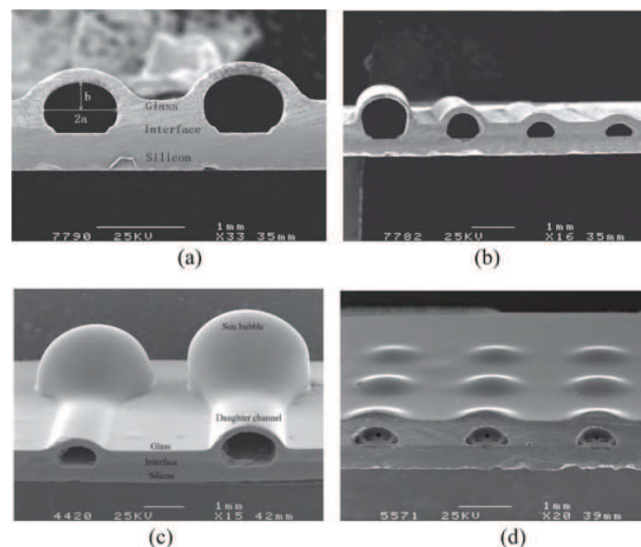


Figure 4: Structures formed in glass bonded to a Si wafer by the action of H_2 gas released from the thermal decomposition of TiH_2 . Reproduced with permission from [54].

Perhaps an even more versatile bubble-related microfabrication strategy has been introduced by DeLouise *et al.* [55–57], as shown in Fig. 5. Polydimethylsiloxane (PDMS) is a Si-based polymer exhibiting tunable mechanical, chemical and optical properties that are widely leveraged in microfluidic and biotechnology applications.

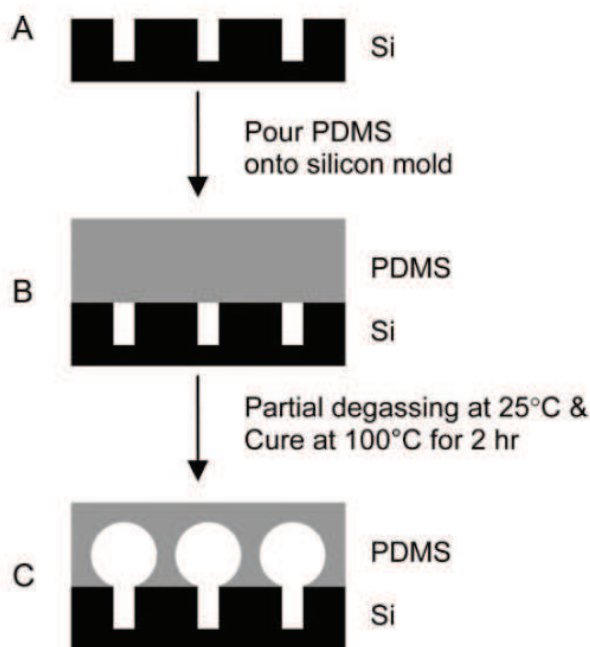


Figure 5: Gentle degassing of PDMS leads to the growth of gas filled cavities at location determined by lithographically processed trenches in a Si mold. Subsequent curing fixes these cavities into the PDMS, which can then be removed from the Si mold so that the cavities can be used as microvials. Reproduced with permission from [55–57].

PDMS is inert and non-toxic, making it well suited for cell culture and tissue engineering applications. However, it is not easily machined. Their technique produces microbubbles, which are spherical cavities formed in thermally cured PDMS using a gas expansion molding technique. The architecture of the microbubble is uniquely advantageous for cell culture. Large format arrays provide a highly versatile system that can be adapted for use in various high-throughput cell-sorting applications.

Their method begins with standard lithographic processing to create a Si wafer mold. Deep reactive ion etching (DRIE) using the Bosch process that consists of sequential SF_6 etching and C_4F_8 passivation steps is used to create pits. Crucially, the hydrophobic coating is retained. The PDMS prepolymer is mixed and cast directly onto the hydrophobic mold. The PDMS is set at room temperature for 15 min to allow for passive degassing rather than performing the usual vacuum degassing. PDMS is then cured at 100°C for 2 h. After curing, the formation of spherical cavities is observed. Gas trapped in the pit under the PDMS pre-mix expanded at high temperature to nucleate vapor bubble formation. Gas dissolved in the PDMS pre-mix diffused

to further the bubble growth. Surface tension pins the microbubble to the lithographically defined pits and prevents detachment of the vapor bubble that forms in the PDMS over the pit. The fabrication parameters that effect the microbubble cavity formation efficiency and size include: (1) the hydrophobic coating of the mold, (2) the mold pit dimensions, (3) the spatial arrangement of the pit openings, (4) the curing temperature of PDMS pre-polymer, (5) PDMS thickness, and (6) the presence and composition of residual gas in the PDMS pre-polymer mixture.

These last two examples show that bubbles can be used for the formation of microcompartments suitable for performing chemical reactions. The question now arises as to whether microcompartments themselves might be able to change the course of reactions. In other words, is chemistry in a bubble different than chemistry in the bulk? This question has been addressed by Fallah-Araghi *et al.* [58], who answer in the affirmative. They demonstrate that both the kinetics and thermodynamics of synthetic reactions can be enhanced by compartmentalization at the mesoscale within micrometer-diameter droplets. This may have particularly interesting implications for chemistry within the prebiotic soup, or what is known as preevolutionary dynamics [59]. This general reaction enhancement scheme also has implications for atmospheric aerosol chemistry and synthetic biology.

Fallah-Araghi *et al.* [58] used the reversible reaction of a nonfluorescent amine with a very weakly fluorescent aldehyde to form a fluorescent imine in water. Microfluidic emulsification produced monodisperse compartments made of aqueous droplets in the picoliter range ($2.5 - 160\text{ pL}$, radius $8 \leq R \leq 34\ \mu\text{m}$) in a fluorinated oil and stabilized by a nonionic surfactant.

One of their first observations was a change in the reaction mechanism with microconfinement. The bulk reaction kinetics was exponential. In droplets the reaction kinetics was slightly sigmoidal. Such a change indicated that the reaction mechanism must have at least two steps and that relative rates of these steps are influence by microconfinement. Both the apparent forward rate constant k_1 and the apparent equilibrium constant K_{eq} were inversely related to the droplet radius, R . The standard Gibbs free energies of the reactants (Rc), transition state (TS), and product (Pr) were calculated from the apparent K_{eq} , k_1 , and reverse rate constant k_{-1} . Imine synthesis became more favorable in droplets than in bulk largely due to the decrease in $G_{Pr}^\circ - G_{Rc}^\circ$, whereas there was almost no change in $G_{Pr}^\circ - G_{TS}^\circ$. Thus, stabilization of the transition state played, at most, a minor role compared to destabilization of the products.

Narayan *et al.* [60] have previously shown that several "on water" reactions are greatly accelerated when carried out in vigorously stirred aqueous suspensions with high interfacial area. This effect could have a related origin, which Fallah-Arghi *et al.* suggest may be related to an improvement in reaction efficiency in droplets caused by transformation of mechanical energy used to form droplets into chemical energy. The observed shift in the chemical equilibrium is $\sim 10 \text{ kJ mol}^{-1}$. This corresponds to a total chemical energy of 10^{-12} J with a concentration of $\sim 0.17 \text{ mM}$ of product. Suggestively, the mechanical work done to create the interface of the 2.5 pL droplet is $w = 4\pi\gamma R^2 \sim 10^{-12} \text{ J}$, the same order of magnitude as the chemical energy.

Fallah-Arghi *et al.* expect the mechanism they describe to be quite general, requiring no size or shape complementarity and only relatively low energy binding of the reactants to the droplet interface. They highlight some similarities with the enhancement of certain reactions in micellar systems. Micelles function as catalysts in some cases, as compared to other cases in which activity coefficient effects are at the root of reactivity enhancement. For many bimolecular reactions, however, the dominant effect is attributed to reactants being concentrated relative to the surrounding water phase through interaction with the micelle surface or insertion into the micelle itself [61, 62]. In the work of Fallah-Arghi *et al.* the reaction thermodynamics in droplets shifted in favor of product formation compared to reaction in bulk solution. The shift is controlled by the dimensionless number $\sqrt{D/(k_{-1}R^2)}$, comparing the typical distance over which a product molecule diffuses in the time given by the reverse rate constant in bulk solvent to the compartment size. For large values of this dimensionless number, i.e., small droplet sizes, the equilibrium constant and the forward reaction rate both scale as $1/R$, leading to a strong increase in synthetic efficiency at small dimension.

4 Conclusion

It is hoped that this broad review will help to familiarize an interdisciplinary audience with the importance and potential usefulness of bubbles and an understanding of bubble dynamics. A classical discussion of nucleation, growth and detachment of bubbles sets the framework for understanding bubble dynamics. Nucleation in practical systems nearly always occurs via nonclassical pathways, which means that the rate of bubble formation is higher than classical predictions. Nonetheless, classical

arguments possess great utility for explaining the necessity for nonclassical pathways as well as the growth and detachment of bubbles. Bubble dynamics has the potential to impact a range of technological and scientific studies, especially if researchers in diverse fields can be made aware of parallel advances. While foaming is widely used for producing porous materials with randomly distributed cavities with a broad size distribution [63, 64], examples are highlighted here in which controlled bubble formation leads to structures exhibiting not only control of the size distribution but also of the position of the cavities so formed. Size- and order-controlled materials will be of increasing importance not only for their designable materials properties but also for their ability to localize and perhaps alter chemical reactivity within their cavities.

Acknowledgement: I thank Yan Delauré, Lisa DeLouise, and Anthony Robinson for providing original copies of their figures for reproduction.

References

- [1] Liger-Belair G., Conreux A., Villaume S., Cilindre C., 2013. Monitoring the losses of dissolved carbon dioxide from laser-etched champagne glasses. *Food Res. Internat.*, 54, 516-522.
- [2] Zhang B. L., Wang J., Li M., Hou Q., 2013. A molecular dynamics study of helium bubble formation and gas release near titanium surfaces. *J. Nucl. Mater.*, 438, 178-182.
- [3] Mostowfi F., Molla S., Tabeling P., 2012. Determining phase diagrams of gas-liquid systems using a microfluidic PVT. *Lab Chip*, 12, 4381-4387.
- [4] Di Bari S., Robinson A. J., 2013. Experimental study of gas injected bubble growth from submerged orifices. *Exp. Thermal Fluid Sci.*, 44, 124-137.
- [5] Albadawi A., Donoghue D. B., Robinson A. J., Murray D. B., De-laure Y. M. C., 2013. On the analysis of bubble growth and detachment at low capillary and bond numbers using volume of fluid and level set methods. *Chem. Eng. Sci.*, 90, 77-91.
- [6] Jones S. F., Evans G. M., Galvin, K. P., 1999. Bubble nucleation from gas cavities - a review. *Adv. Colloid Interface Sci.*, 80, 27-50.
- [7] Lubetkin S. D., 1989. The nucleation and detachment of bubbles. *J. Chem. Soc., Faraday Trans.*, 85, 1753-1764.
- [8] Lugli F., Zerbetto F., 2007. An introduction to bubble dynamics. *Phys. Chem. Chem. Phys.*, 9, 2447-2456.
- [9] Bang J. H., Suslick K. S., 2010. Applications of ultrasound to the synthesis of nanostructured materials *Adv. Mater.*, 22, 1039-1059.
- [10] Suslick K. S., Price G. J., 1999. Applications of ultrasound to materials chemistry. *Annu. Rev. Mater. Sci.*, 29, 295-326.
- [11] Xu H. X., Zeiger B. W., Suslick K. S., 2013. Sonochemical synthesis of nanomaterials. *Chem. Soc. Rev.*, 42, 2555-2567.
- [12] Gedanken A., 2008. Preparation and properties of proteinaceous microspheres made sonochemically. *Chemistry*, 14,

- 3840-3853.
- [13] Skirtenko N., Tzanov T., Gedanken A., Rahimipour S., 2010. One-step preparation of multifunctional chitosan microspheres by a simple sonochemical method. *Chemistry*, 16, 562-567.
- [14] Gabashvili A., Major D. T., Perkas N., Gedanken A., 2010. The sonochemical synthesis and characterization of mesoporous chiral titania using a chiral inorganic precursor. *Ultrason. Sonochem.*, 17, 605-609.
- [15] Belova V., Borodina T., Mohwald H., Shchukin D. G., 2011. The effect of high intensity ultrasound on the loading of Au nanoparticles into titanium dioxide. *Ultrason. Sonochem.*, 18, 310-317.
- [16] Okorn-Schmidt H. F., Holsteyns F., Lippert A., Mui D., Kawaguchi M., Lechner C., Frommhold P. E., Nowak T., Reuter F., Pique M. B., Cairo C., Mettind R., 2014. Particle cleaning technologies to meet advanced semiconductor device process requirements. *ECS J. Solid State Sci. Technol.*, 3, N3069-N3080.
- [17] Hernot S., Klibanov A. L., 2008. Microbubbles in ultrasound-triggered drug and gene delivery. *Adv. Drug Deliv. Rev.*, 60, 1153-1166.
- [18] Dapkus K. V., Sides P. J., 1986. Nucleation of electrolytically evolved hydrogen at an ideally smooth electrode. *J. Colloid Interface Sci.*, 111, 133-151.
- [19] Huang W. J., Manjare M., Zhao Y. P., 2013. Catalytic nanoshell micromotors. *J. Phys. Chem. C*, 117, 21590-21596.
- [20] Manesh K. M., Cardona M., Yuan R., Clark M., Kagan D., Balasubramanian S., Wang J., 2010. Template-assisted fabrication of salt-independent catalytic tubular microengines. *ACS Nano*, 4, 1799-1804.
- [21] Hornberger H., Virtanen S., Boccaccini A. R., 2012. Biomedical coatings on magnesium alloys - A review. *Acta Biomater.*, 8, 2442-2455.
- [22] Kim Y. K., Park I. S., Lee S. J., Lee, M. H., 2013. Biodegradation and cytotoxic properties of pulse anodized Mg alloys. *Met. Mater. Int.*, 19, 353-360.
- [23] Virtanen S., 2011. Biodegradable Mg and Mg alloys: Corrosion and biocompatibility. *Mater. Sci. Eng. B*, 176, 1600-1608.
- [24] Killian M. S., Wagener V., Schmuki P., Virtanen S., 2010. Functionalization of metallic magnesium with protein layers via linker molecules. *Langmuir*, 26, 12044-12048.
- [25] Wagener V., Killian M. S., Turhan C. M., Virtanen S., 2013. Albumin coating on magnesium via linker molecules-Comparing different coating mechanisms. *Colloids Surf. B*, 103, 586-594.
- [26] Aghion E., Levy G., Ovadia S., 2012. In vivo behavior of biodegradable Mg-Nd-Y-Zr-Ca alloy. *J. Mater. Sci. Mater. Med.*, 23, 805-812.
- [27] Staiger M. P., Pietak A. M., Huadmai J., Dias G., 2006. Magnesium and its alloys as orthopedic biomaterials: A review. *Biomaterials*, 27, 1728-1734.
- [28] Shafer N. E., Zare R. N., 1991. Through a beer glass darkly. *Phys. Today*, 44, 48-52.
- [29] Shafer N. E., Zare R. N., 1992. Ferment over beer bubbles - reply. *Phys. Today*, 45, 112.
- [30] Volmer M., 1929. Über Keimbildung und Keimwirkung als Spezialfälle der heterogenen Katalyse. *Z. Elektrochem.*, 35, 555-561.
- [31] Fletcher N. H., 1958. Size Effect in heterogeneous nucleation. *J. Chem. Phys.*, 29, 572-576.
- [32] Qian M., Ma J., 2009. Heterogeneous nucleation on convex spherical substrate surfaces: A rigorous thermodynamic formulation of Fletcher's classical model and the new perspectives derived. *J. Chem. Phys.*, 130, 214709.
- [33] Adamson A. W., Gast A. P., 1997. *Physical Chemistry of Surfaces*, New York, John Wiley & Sons.
- [34] Metiu H., 2006. *Physical Chemistry: Thermodynamics*, New York, Taylor, Francis.
- [35] Nagashima G., Levine E. V., Hoogerheide D. P., Burns M. M., Golovchenko J. A., 2014. Superheating and homogeneous single bubble nucleation in a solid-state nanopore. *Phys. Rev. Lett.*, 113, 024506.
- [36] Liger-Belair G., 2012. The physics behind the fizz in champagne and sparkling wines. *Euro. Phys. J.-Special Topics*, 201, 1-88.
- [37] Liger-Belair G., Polidori G., Jeandet P., 2008. Recent advances in the science of champagne bubbles. *Chem. Soc. Rev.*, 37, 2490-2511.
- [38] Lesage F. J., Cotton J. S., Robinson A. J., 2013. Analysis of quasi-static vapour bubble shape during growth and departure. *Phys. Fluids*, 25, 067103.
- [39] Amouzgar M., Kahrizi M., 2012. A new approach for improving the silicon texturing process using gas-lift effect. *J. Phys. D: Appl. Phys.*, 45, 105102.
- [40] Xie X. Z., Hu M. F., Chen W. F., Wei X., Hu W., Gao X. Y., Yuan X. R., Hong M. H., 2013. bubble dynamics during laser wet etching of transparent sapphire substrates by 1064 nm laser irradiation. *J. Laser Micro Nanoeng.*, 8, 259-265.
- [41] Vu Q.-B., Stricker D. A., Zavracky P. M., 1996. Surface characteristics of (100) silicon anisotropically etched in aqueous KOH. *J. Electrochem. Soc.*, 143, 1372-1375.
- [42] Zubel I., Kramkowska M., 2001. The effect of isopropyl alcohol on etching rate and roughness of (100) Si surface etched in KOH and TMAH solutions. *Sens. Actuators A*, 93, 138-147.
- [43] Zubel I., Kramkowska M., 2002. The effect of alcohol additives on etching characteristics in KOH solutions. *Sens. Actuators A*, 101, 255-261.
- [44] Yang C.-R., Yang C.-H., Chen P.-Y., 2005. Study on anisotropic silicon etching characteristics in various surfactant-added tetramethyl ammonium hydroxide water solutions. *J. Microchem. Microeng.*, 15, 2028-2037.
- [45] Aldinger B. S., Gupta A., Clark I. T., Hines M. A., 2010. The same etchant produces both near-atomically flat and microfaceted Si(100) surfaces: The effects of gas evolution on etch morphology. *J. Appl. Phys.*, 107, 103520.
- [46] Clark I. T., Aldinger B. S., Gupta A., Hines M. A., 2010. Aqueous etching produces Si(100) surfaces of near-atomic flatness: Strain minimization does not predict surface morphology. *J. Phys. Chem. C*, 114, 423-428.
- [47] Hines M. A., Faggin M. F., Gupta A., Aldinger B. S., Bao K., 2012. Self-propagating reaction produces near-ideal functionalization of Si(100) and flat surfaces. *J. Phys. Chem. C*, 116, 18920-18929.
- [48] Pauric A. D., Baig S. A., Pantaleo A. N., Wang Y., Kruse P., 2013. Sponge-like porous metal surfaces from anodization in very concentrated acids. *J. Electrochem. Soc.*, 160, C12-C18.
- [49] Moutanabbir O., Gösele U., 2010. Heterogeneous integration of compound semiconductors. *Annu. Rev. Mater. Res.*, 40, 469-500.

- [50] De La Rosa C. J. L., Sun J., Lindvall N., Cole M. T., Nam Y., Loffler M., Olsson E., Teo K. B. K., Yurgens A., 2013. Frame assisted H₂O electrolysis induced H₂ bubbling transfer of large area graphene grown by chemical vapor deposition on Cu. *Appl. Phys. Lett.*, 102, 022101.
- [51] Gao L., Ren W., Xu H., Jin L., Wang Z., Ma T., Ma L.-P., Zhang Z., Fu Q., Peng L.-M., Bao X., Cheng H.-U., 2012. Repeated growth and bubbling transfer of graphene with millimetre-size single-crystal grains using platinum. *Nat. Commun.*, 3, 699.
- [52] Gao L. B., Ni G. X., Liu Y. P., Liu B., Neto A. H. C., Loh K. P., 2014. Face-to-face transfer of wafer-scale graphene films. *Nature (London)*, 505, 190-194.
- [53] Chevalier E., Chulia D., Pouget C., Viana M., 2008. Fabrication of porous substrates: A review of processes using pore forming agents in the biomaterial field. *J. Pharm. Sci.*, 97, 1135-1154.
- [54] Shang J. T., Chen B. Y., Lin W., Wong C. P., Zhang D., Xu C., Liu J. W., Huang Q. A., 2011. Preparation of wafer-level glass cavities by a low-cost chemical foaming process (CFP). *Lab Chip*, 11, 1532-1540.
- [55] Bobo B., Phelan D., Rebhahn J., Piepenbrink M. S., Zheng B., Mosmann T. R., Kobie J. J., Delouise L. A., 2014. Microbubble array diffusion assay for the detection of cell secreted factors. *Lab on a Chip*, 14, 3640-3650.
- [56] Giang U. B. T., Jones M. C., Kaule M. J., Virgile C. R., Pu Q. H., Delouise L. A., 2014. Quantitative analysis of spherical microbubble cavity array formation in thermally cured polydimethylsiloxane for use in cell sorting applications. *Biomed. Microdevices*, 16, 55-67.
- [57] Giang U. B. T., Lee D., King M. R., Delouise L. A., 2007. Microfabrication of cavities in polydimethylsiloxane using DRIE silicon molds. *Lab Chip*, 7, 1660-1662.
- [58] Fallah-Araghi A., Meguellati K., Baret J. C., El Harrak A., Mangeat T., Karplus M., Ladame S., Marques C. M., Griffiths A. D., 2014. Enhanced chemical synthesis at soft interfaces: A universal reaction-adsorption mechanism in microcompartments. *Phys. Rev. Lett.*, 112, 028301.
- [59] Chen I. A., Nowak M. A., 2012. From Prolife to Life: How Chemical Kinetics Become Evolutionary Dynamics. *Acc. Chem. Res.*, 45, 2088-2096.
- [60] Narayan S., Muldoon J., Finn M. G., Fokin V. V., Kolb H. C., Sharpless K. B., 2005. "On water": Unique reactivity of organic compounds in aqueous suspension *Angew. Chem., Int. Ed. Engl.*, 44, 3275-3279.
- [61] Cordes E. H., 2009. Kinetics of organic reactions in micelles. *Pure Appl. Chem.*, 50, 617-625.
- [62] Dwars T., Paetzold E., Oehme G., 2005. Reactions in Micellar Systems. *Angew. Chem., Int. Ed. Engl.*, 44, 7174-7199.
- [63] Karimi M., Heuchel M., Weigel T., Schossig M., Hofmann D., Lendlein A., 2012. Formation and size distribution of pores in poly(epsilon-caprolactone) foams prepared by pressure quenching using supercritical CO₂. *J. Supercrit. Fluid.*, 61, 175-190.
- [64] Shafi M. A., Joshi K., Flumerfelt R. W., 1997. Bubble size distributions in freely expanded polymer foams. *Chem. Eng. Sci.*, 52, 635-644.
- [65] Chen Y., Zhang S., Li J., Song Y., Zhao C., Zhang X., 2010. Dynamic degradation behavior of MgZn alloy in circulating m-SBF. *Mater. Lett.*, 64, 1996-1999.
- [66] Degner J., Singer F., Cordero L., Boccaccini A. R., Virtanen S., 2013. Electrochemical investigations of magnesium in DMEM with biodegradable polycaprolactone coating as corrosion barrier. *Appl. Surf. Sci.*, 282, 264-270.